Colossal optical anisotropy from atomic-scale modulations

Hongyan Mei[1†], Guodong Ren[2†], Boyang Zhao[3†], Jad Salman[1†], Gwan Yeong Jung[4], Huandong Chen[3], Shantanu Singh[3], Arashdeep S. Thind[2], John Cavin[5], Jordan A. Hachtel[6], Miaofang Chi[6], Shanyuan Niu[3], Graham Joe[1], Chenghao Wan[1,7], Nick Settineri[8], Simon J. Teat[8], Bryan C. Chakoumakos[9], Jayakanth Ravichandran[3,10,11*], Rohan Mishra[2,4*], Mikhail A. Kats[1,7*]

[1] *Department of Electrical and Computer Engineering, University of Wisconsin-Madison, Madison, WI 53706, USA*

[2] *Institute of Materials Science and Engineering, Washington University in St. Louis, St. Louis, MO 63130, USA* [3] *Mork Family Department of Chemical Engineering and Materials Science, University of Southern California, Los Angeles, CA 90089, USA*

[4] *Department of Mechanical Engineering and Material Science, Washington University in St. Louis, St. Louis, MO 63130, USA*

[5] *Department of Physics, Washington University in St. Louis, St. Louis, MO 63130, USA*

[6] *Center for Nanophase Materials Sciences, Oak Ridge National Laboratory, Oak Ridge, TN 37831, USA*

[7] *Department of Materials Science and Engineering, University of Wisconsin-Madison, Madison, WI 53706, USA*

[8] *Advanced Light Source, Lawrence Berkeley National Laboratory, Berkeley, CA 94720, USA* [9] *Neutron Scattering Division, Oak Ridge National Laboratory, Oak Ridge TN 37831, USA*

[10] *Ming Hsieh Department of Electrical Engineering, University of Southern California, Los Angeles, CA 90089, USA*

[11] *Core Center for Excellence in NanoImaging, University of Southern California, Los Angeles, CA 90089, USA*

[†] *These authors contributed equally to this work*

**Email: mkats@wisc.edu, rmishra@wustl.edu, jayakanr@usc.edu*

Keywords: optical anisotropy, birefringence, chalcogenide, structural modulation, STEM

Summary paragraph

In modern optics, materials with large birefringence (, where is the refractive index) are sought after for polarization control (*e.g.* in wave plates, polarizing beam splitters, etc.[1–3]), nonlinear optics and quantum optics (*e.g.* for phase matching[4,5] and production of entangled photons[6]), micromanipulation[7], and as a platform for unconventional light-matter coupling, such as Dyakonov-like surface polaritons[8] and hyperbolic phonon polaritons[9–11]. Layered ―van der Waals‖ materials, with strong intra-layer bonding and weak inter-layer bonding, can feature some of the largest optical anisotropy[12–16]; however, their use in most optical systems is limited because their optic axis is out of the plane of the layers and the layers are weakly attached, making the anisotropy hard to access. Here, we demonstrate that a bulk crystal with subtle periodic modulations in its structure — $Sr_{9/8}TiS_3$ — is transparent and positive-uniaxial, with extraordinary index and ordinary index in

the mid- to far-infrared. The excess Sr, compared to stoichiometric $SrTiS_3$, results in the formation of TiS_6 trigonal-prismatic units that break the infinite chains of face-shared TiS_6 octahedra in $SrTiS_3$ into periodic blocks of five TiS_6 octahedral units. The additional electrons introduced by the excess Sr subsequently occupy the TiS_6 octahedral blocks to form highly oriented and polarizable electron clouds, which selectively boost the extraordinary index and result in record birefringence (with low loss). The connection between subtle structural modulations and large changes in refractive index suggests new categories of anisotropic materials and also tunable optical materials with large refractive-index modulation and low optical losses.

Main text

Birefringence is the dependence of the refractive index on the polarization of light travelling through a material. The observation of birefringence in calcite as early as 1669[17]—called Iceland spar at the time—eventually led to Fresnel's insight in 1821 that light is a transverse wave[18,19]. Calcite's record as the most birefringent material stood for over a century, with | | in the visible, as analyzed and explained by Bragg[20]; here, and are respectively the extraordinary and ordinary refractive index. In calcite ($CaCO_3$) and other calcite-type carbonates (RCO_3; R = Mg, Zn, Fe, Mn, and others), the anisotropy primarily results from the interaction of dipole excitations around the oxygen atoms within the planar carbonate ions (CO_3^{2-}), which are all oriented perpendicular to the optic axis within the crystal[20–23]. Achieving much larger optical birefringence is expected to require much larger structural anisotropy.

Indeed, the revolution of layered (two-dimensional or 2D) materials has led to the demonstration of many crystals with very large optical anisotropy due to strong intra-layer bonding (covalent or ionic) and weak inter-layer bonding (van der Waals), resulting in, e.g., in hexagonal boron nitride (h-BN)[13] in the visible and near infrared and in molybdenum disulfide (MoS_2)[16] in the near infrared [Fig. 1(e, f)]. However, the giant anisotropy found in (usually thin) layered crystals is difficult to exploit for either bulk optics or micro-optics because their optic axis is out of the plane of the layers and the layers are weakly bonded. Therefore, there is a need to discover or engineer bulk materials with giant anisotropy, especially in the infrared. In 2018, our groups[i] reported that $BaTiS_3$, a quasi-one-dimensional (quasi-1D) hexagonal perovskite chalcogenide with face-shared (TiS_6) octahedral chains, has at mid-infrared frequencies where it is transparent—a record at the time[24,25]. These quasi-1D hexagonal chalcogenide single crystals[26] and thin films[27] can be grown with different orientations to enable easy access to their anisotropic properties. Therefore, they are an attractive and largely unexplored class of materials to achieve higher birefringence and dichroism. At the time, we selected Ba, S, and Ti ions and studied $BaTiS_3$ due to the large contrast in the electronic

[i] Only some authors overlap between the two papers

polarizability of the individual candidate ions in the ABX_3 quasi-1D structure, and thus believed that the birefringence we demonstrated is close to the limit for this class of materials[24].

Here, we introduce structural modulation as a new mechanism for dramatically enhancing the anisotropy of electronic polarizability, far exceeding values that have been achievable by the anisotropic distribution of individual ions with distinct polarizability. In quasi-1D chalcogenide $Sr_{1+x}TiS_3$, the structural modulation controls the selective occupation of strongly oriented (anisotropic) electronic states, and hence leads to a birefringence of ~ 2.1, significantly larger than has been observed in transparent regions of both quasi-1D and layered ―van der Waals‖ materials to date [Fig. 1(e, f)].

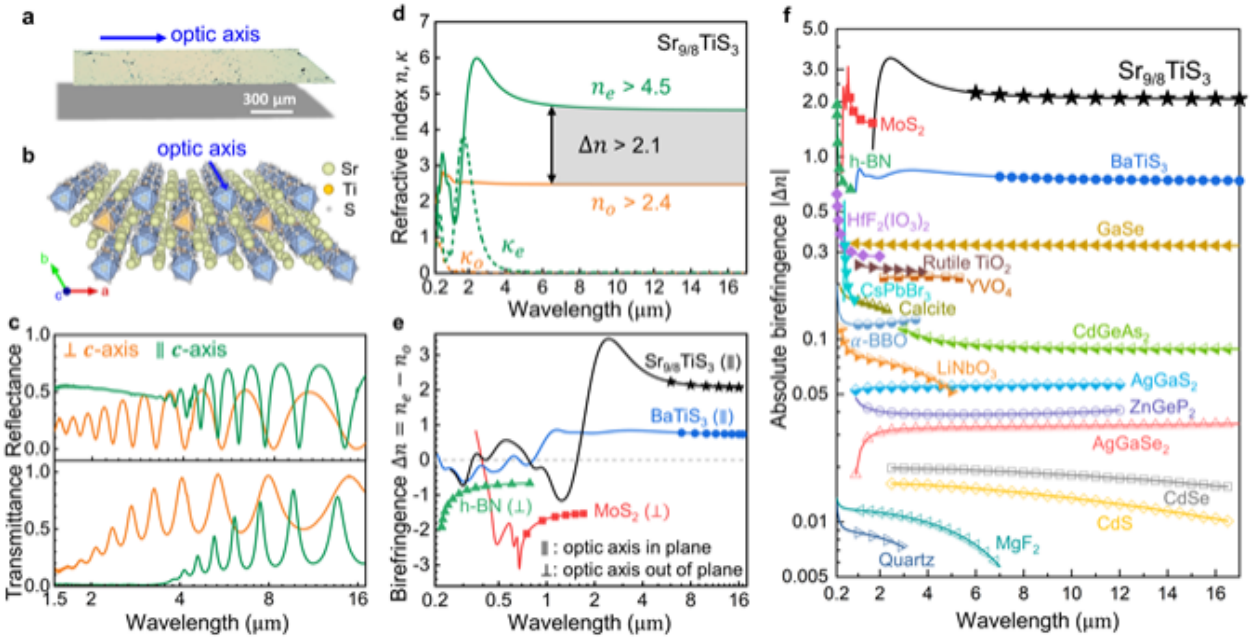

Figure 1. Infrared birefringence in $Sr_{9/8}TiS_3$ single crystals. a. Optical image of the $Sr_{9/8}TiS_3$ crystal measured in this work, with scale bar. **b**. Perspective schematic of a $Sr_{9/8}TiS_3$ crystal with the optic axis along the TiS_6 chains. **c**. Polarized reflectance and transmittance of a $Sr_{9/8}TiS_3$ crystal plate with thickness = 3.2 μm measured across the mid infrared (the wavelength axis uses the log scale). **d**. Extracted complex refractive-index values of uniaxial $Sr_{9/8}TiS_3$ for the ordinary (perpendicular to *c*-axis, orange) and extraordinary (parallel to *c*-axis, green) directions spanning the visible through the mid infrared, based on a combination of spectroscopic ellipsometry and transmittance/reflectance measurements. For wavelengths longer than 6 μm, the material is highly transparent and maintains a large birefringence, $\Delta n > 2.1$ (gray shaded region). **e.** Comparison of the birefringence of two representative hexagonal quasi-1D chalcogenides ($Sr_{9/8}TiS_3$ and $BaTiS_3$[24]) with highly anisotropic 2D materials (h-BN[13] and MoS_2[16]). The transparent regions of these materials are identified using symbols. **f.** Comparison of the absolute birefringence values of $Sr_{9/8}TiS_3$ and a variety of anisotropic materials [from the literature[13,16,24,28–37]], showing that $Sr_{9/8}TiS_3$ has by far the largest birefringence among reported anisotropic crystals. The symbols indicate regions of transparency.

Synthesis and basic structure of strontium titanium sulfide crystals

We synthesized single crystals of $Sr_{9/8}TiS_3$ using the chemical vapor transport method, which has been reported earlier[24,26,38,39]. $Sr_{1+x}TiS_3$ falls in a broad category of $BaNiO_3$-related structures, with chemical formula $A_{1+x}BX_3$ (A = alkaline metal, B = transition metal, X = anion)[40,41]. It has quasi-1D chains of face-shared BX_6 octahedra that are aligned along a 6-fold rotational axis (commonly the c-axis) with A cations filling the inter-chain interstitials. Its chemical composition was determined to be off-stoichiometric using energy dispersive analytical X-ray spectroscopy (EDS) as reported in a previous work[39]. Although $A_{1+x}BX_3$ compounds are commonly stoichiometric (i.e., $x = 0$), certain non-stoichiometric crystalline structures, such as $Sr_{9/8}TiS_3$ and $Sr_{8/7}TiS_3$, have been reported to be more thermodynamically stable[42,43]; in these structures, excess Sr atoms periodically compress the Sr-lattice while introducing a stacking sequence of distorted TiS_6 polyhedral and displaced Sr atoms along the c-axis, expressed as structural modulation[40,42,43].

Measurement of colossal birefringence

The optical anisotropy of $Sr_{9/8}TiS_3$ was measured in two steps: we first acquired polarization-dependent, normal-incidence reflectance and transmittance spectra of the plate in Fig. 1(a) using Fourier-transform infrared spectroscopy (FTS), shown in Fig. 1(c). The thickness of the crystal was estimated to be 3.2 m by fitting to the Fabry–Pérot fringes in the spectra for each polarization, and verified by cross-section scanning electron microscope (SEM) imaging (Fig. S3 in *Supplementary Section 2*). The large difference in the reflectance and transmittance between the two polarizations (parallel and perpendicular to the c-axis) is a clear indication of large optical anisotropy. For wavelengths longer than ~6 m, we observe low optical losses up to the cut-off wavelength of the detector at 17 m [Fig. 1(d)]. We expect that this low-loss region extends to longer wavelengths, limited by phonon (~27 m)[39] or plasmon resonance (~100 m, calculated in *Supplementary Section 2*).

To fully quantify the degree of optical anisotropy, we then combined variable-angle ellipsometry measurements over the spectral range of 210 nm to 2500 nm with the polarization-resolved reflection and transmission measurements in Fig. 1(c), and extracted the complex refractive index of $Sr_{9/8}TiS_3$ for wavelengths from 210 nm to 17 m [Fig. 1(d)]. Three different ellipsometry measurement were performed: with the c-axis parallel to the plane of incidence, perpendicular to the plane of incidence, and at an off-axis angle; all of this data was combined in a simultaneous analysis (*see more details in Supplementary Section 2*). In the low-loss region of 6 m, $Sr_{9/8}TiS_3$ has a birefringence ( ) up to 2.1. This is by far the largest birefringence among reported anisotropic crystals, to the best of our knowledge [Fig. 1(f)]. Compared to layered 2D materials MoS_2[16] and h-BN[13], $Sr_{9/8}TiS_3$ possesses large anisotropy across a broad low-loss region in mid-infrared [Fig. 1(e)], and the in-plane optic axis is easy to exploit for practical optical components. As we discuss below, this extreme birefringence is

a result of the enhancement of the extraordinary index ( ) from the expected 3.4 in a hypothetical unmodulated stoichiometric crystal to ~4.5 in $Sr_{9/8}TiS_3$.

Direct observation of structural modulations in $Sr_{9/8}TiS_3$ crystals

The crystal structure of $Sr_{9/8}TiS_3$ was resolved using single-crystal X-ray diffraction (SC-XRD). Both 3D and (3+1)D modulation approaches were used to solve the modulated structure (*Supplementary Section 1*). The resulting $Sr_{54}Ti_{48}S_{144}$ structure of *R*3*c* and $Sr_{1.125}TiS_3$ structure of *R*3*m*(00g)0*s*[44] space groups reveal a similar modulated structure (visualized in Fig. 2(a, b)), which is consistent with the previously reported *R*3*m*(00g)0*s* $Sr_{9/8}TiS_3$ structure[42,43,45–47]. The details of the data collection, data reduction, and structure refinements are listed in Tables S1 in *Supplementary Section 1*, and the best resulting crystal structure is reported in Table S2 and Table S3 in *Supplementary Section 1*.

In contrast to the hypothetical stoichiometric counterpart $SrTiS_3$ (*Supplementary Section 3* Fig. S8), the $Sr_{9/8}TiS_3$ lattice has structural modulations consisting of blocks of face-shared octahedra (referred as _O‘) that are separated by pseudo-trigonal-prismatic TiS_6 units (referred as _T‘) along the *c*-axis as shown in Fig. 2(b). The structural modulation of $Sr_{9/8}TiS_3$ arises from an overall trigonal twist distortion compared to the average unmodulated structure of $SrTiS_3$. To accommodate excess Sr in the lattice along the *c*-axis, Sr atoms undergo displacements within the *ab* plane, resulting in the triangular-shaped projection in Fig. 2(a). The Sr displacements are accompanied by twist distortion of TiS_6 units from octahedral to trigonal-prismatic polyhedra. These different polyhedral units have different Ti–Ti distances along the *c*-axis (Fig. S9 and S10 in *Supplementary Section 5*). By counting the stacking sequence of building blocks (structurally classified as O and T), TiS_6 chains with periodic $[-(T-O-T)\ -(O)_5-]_2$ succession can be used to define the modulation periodicity of 16 units of TiS_6 within every 18 Sr layers in the $Sr_{9/8}TiS_3$ lattice [Fig. 2(b)].

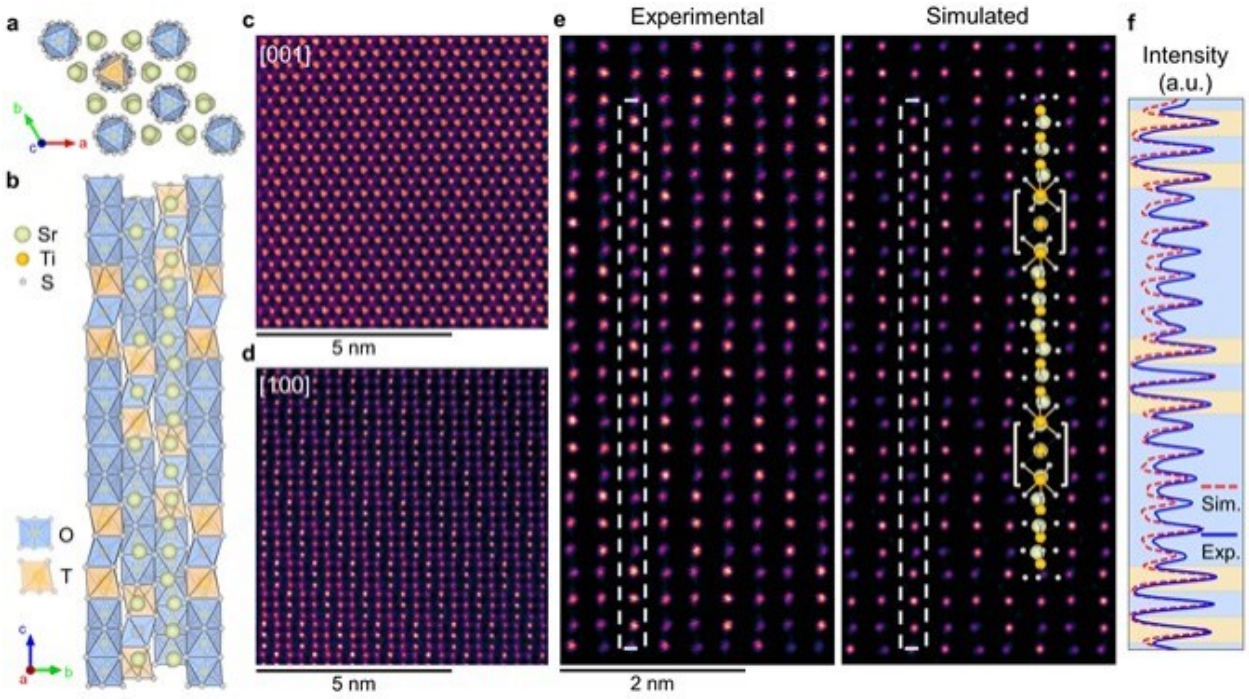

Figure 2. Structural modulation in $Sr_{9/8}TiS_3$. a, b. Schematics representing the modulated $Sr_{9/8}TiS_3$ (*R*3*c*) lattice, resolved from single-crystal XRD (SC-XRD), and viewed along the [001] axis in **a**, and [100] axis in **b**. The octahedral (O) and pseudo-trigonal prismatic (T) TiS_6 units are highlighted in blue and orange, respectively. **c, d.** Atomic-resolution HAADF-STEM images of a $Sr_{9/8}TiS_3$ crystal along the [001] axis in **c**, and [100] axis in **d**. **e.** High-magnification HAADF-STEM image (left panel) and simulated image (right panel) of $Sr_{9/8}TiS_3$ view along the [100] axis. A schematic of one column of atoms is overlayed on the simulated image. A repeating pattern of three bright atomic columns, where the Ti and Sr atoms overlap along the viewing direction, can be observed in these HAADF images. These triplet atomic columns are highlighted with square brackets in the atomic model. **f.** Line profiles across the experimental and simulated STEM images (white boxes in **e**) comparing the intensity variation across a single atomic column.

To directly visualize the subtle structural modulations in $Sr_{9/8}TiS_3$, we performed atomically resolved imaging using an aberration-corrected scanning transmission electron microscope (STEM). Large field-of-view, high-angle annular dark-field (HAADF) images of the $Sr_{9/8}TiS_3$ crystal viewed along the [001] and [100] zone axis are shown in Fig. 2(c, d). In this imaging mode, the intensity of the atomic columns is approximately proportional to the square of the effective atomic number of the column (Z^2)[48]. Along the [001] zone axis, the Sr atomic columns appear as triangles due to their staggered arrangement along the *c*-axis [Fig. 2(c)], which match well with the structural features in Fig. 2(a). Along the [100] orientation, the Ti and Sr columns overlap within the triple blocks of – (T–O–T) –, and therefore, they appear as bright triplets in the HAADF images as they have higher intensity than the Sr-only atomic columns within the block of five octahedral units $–(O)_5–$ [Fig. 2(d, e)]. We also observe periodic distortions of the Sr atomic columns in the form of contraction and dilation of the Sr–Sr distance between neighboring chains (see more discussions in *Supplementary*

Section 5). A comparison of the intensity and spacing between atomic columns in the experimental and the simulated HAADF images, as shown in Fig. 2(f), shows excellent agreement, and corroborates the modulation periodicity.

Electronic structure and calculation of dielectric properties

To reveal the origin of the giant optical anisotropy in $Sr_{9/8}TiS_3$ and its relationship with structural modulations, we performed first-principles density-functional theory (DFT) calculations. To understand the formation of the modulated $Sr_{9/8}TiS_3$ phase instead of $SrTiS_3$, we performed a convex hull analysis using the DFT calculated energies of the two compounds and all possible lower-order decomposition products (*Supplementary Section 4* Table S5). We find that modulated $Sr_{9/8}TiS_3$ is on the hull, and is thus stable against decomposition, as opposed to stoichiometric $SrTiS_3$, which is thermodynamically metastable, being 45 meV/atom above the hull.

Next, we calculated the electronic structures of $Sr_{9/8}TiS_3$ and $SrTiS_3$ to understand the effect of modulations on the optical properties. Both $SrTiS_3$ and $Sr_{9/8}TiS_3$ are computed to possess an indirect bandgap. $SrTiS_3$ has an indirect bandgap between valence band maximum (VBM) at Γ point and conduction band minimum (CBM) at A point. The topmost valence band and bottom of the conduction band of $SrTiS_3$ show a relatively flat behavior along all the paths in the Brillouin zone, except for the Γ−Z direction, which in the reciprocal space corresponds to the direction parallel to the *c*-axis where the neighboring TiS_6 octahedra have face-sharing connectivity, while octahedral connectivity is broken along the *ab*-plane[49,50]. Compared with $SrTiS_3$, $Sr_{9/8}TiS_3$ shows similarly flat bands. The topmost valence bands and bottom conduction bands arise from *d*-states, and form the indirect bandgap between VBM at Γ and CBM at T.

In $Sr_{9/8}TiS_3$, the electrons introduced by excess Sr^{2+} cations occupy the nominally empty Ti *d* states. Using DFT + Hubbard *U* calculations[51], with a U = 3.0 eV for the Ti atoms, we checked for different magnetic orderings of the moments and found the paramagnetic configuration to be the most stable. The details of the calculations can be found in *Methods* and *Supplementary Section 8*. As shown in the calculated band structure of $Sr_{9/8}TiS_3$ in Fig. 3(b), the additional valence electrons preferentially occupy 3 states (highlighted in red) of Ti atoms in $Sr_{9/8}TiS_3$. These selectively occupied energy states in modulated $Sr_{9/8}TiS_3$ can be corroborated by atomic-resolution electron energy-loss spectroscopy (EELS), which exhibits subtle but distinct differences between the pseudo-trigonal prismatic TiS_6 units (T) and the octahedral TiS_6 units (O) (*Supplementary Section 7* Fig. S14). Compared to the pseudo-trigonal prismatic TiS_6 units (T), octahedral TiS_6 units (O) have shorter Ti-Ti distance, resulting in states that are lower in energy. Thus, the Ti atoms in the O block preferentially accept the additional electrons (*Supplementary Section 6* Fig. S13). This also opens up a

band gap between the occupied 3 states of the octahedrally coordinated Ti atoms and the unoccupied Ti-3 states of the Ti atoms with trigonal-prismatic coordination. The character of the edge states in modulated $Sr_{9/8}TiS_3$ is in sharp contrast to that of $SrTiS_3$ wherein the band gap is between the S-3*p* states in the valence band and Ti-3 states in the conduction band [Fig. 3(a)].

With the electronic ground states computed, we then calculated the complex dielectric function ( ) ( ) ( ) for electric fields along (||) and perpendicular to (⊥) the *c*-axis. The imaginary part $\varepsilon_2(\omega)$ is obtained by calculating the direct transitions between occupied and unoccupied states[52]. The real part $_1(\omega)$ is then extracted by a Kramers-Kronig transformation (see details in *Supplementary Section 8*). Fig. 3(e-f) show the frequency-dependent dielectric functions of the stoichiometric $SrTiS_3$ and the modulated $Sr_{9/8}TiS_3$, with very similar results perpendicular to the *c*-axis ( ), but dramatic enhancement of the dielectric function parallel to the *c*-axis ( ). The enhancement is a consequence of the selective occupation of states at the $(O)_5$ segments in modulated $Sr_{9/8}TiS_3$, which we show in real space by using an isosurface plot of the charge density arising from the occupied 3 band [Fig. 3(d)]. The occupied 3 electrons form a highly oriented blob and result in additional polarizability along the optic axis ( ). In contrast, the electrons from the valence band states in stoichiometric $SrTiS_3$ have an isotropic character and are localized on the S atoms [Fig. 3(c)]. The unoccupied conduction band is at substantially higher energy compared to the 3 electrons, resulting in very few free carriers and therefore low free-carrier absorption.

While an experimental comparison between $Sr_{9/8}TiS_3$ and $SrTiS_3$ cannot be made due to the metastable nature of $SrTiS_3$, we did compare the optical properties of $Sr_{9/8}TiS_3$ to $BaTiS_3$, and to hypothetical $SrTiS_3$ which is isostructural to $BaTiS_3$ in Fig. S19 in *Supplementary Section 8.*

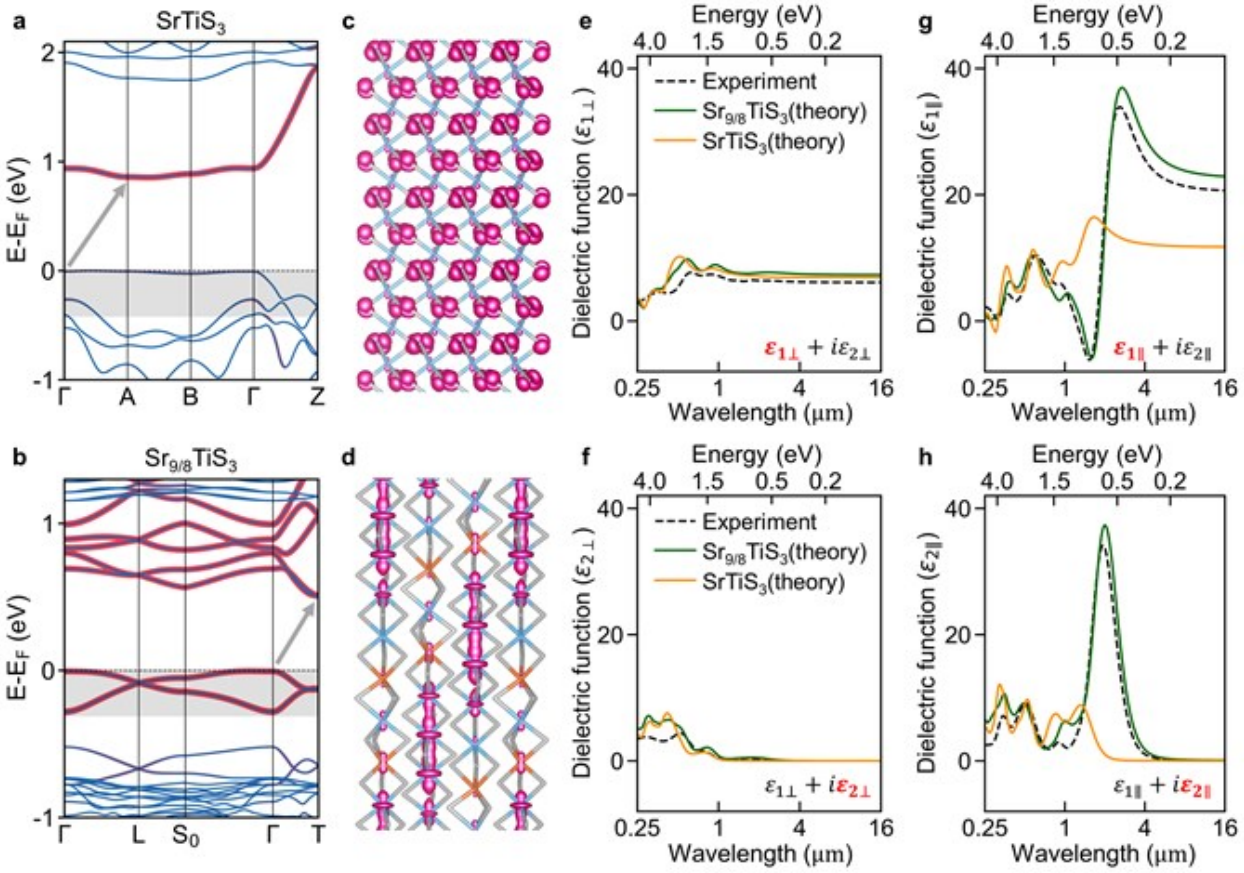

Figure 3. Electronic structure and optical properties of modulated $Sr_{9/8}TiS_3$. a-b. Orbital-projected band structures for hypothetical stoichiometric $SrTiS_3$ in **a**, and modulated $Sr_{9/8}TiS_3$ in **b**. The thicker lines highlighted in red correspond to the contribution from Ti-3 states. The Fermi energy is set to 0 eV. **c-d**. Spatial distribution of the valence electrons below the Fermi energy (shaded in gray in a-b), showing **c.** S-3*p* character in $SrTiS_3$ and **d.** Ti-3 character in $Sr_{9/8}TiS_3$. The isosurface is set to an electron density of 0.004 e/Å^3). **e-h**. Calculated complex dielectric function for polarization perpendicular ( ) and parallel ($_{||}$) to the *c*-axis of the hypothetical stoichiometric $SrTiS_3$ and modulated $Sr_{9/8}TiS_3$, compared to the experimental results (black dashed line). The index = 1 represents the real part of the dielectric function and 2 represents the imaginary part.

Conclusion

In this article, we demonstrate how subtle atomic-scale structural modulations of a bulk crystal can dramatically change its optical properties. We synthesized and studied single-crystal plates of modulated quasi-1D chalcogenide $Sr_{9/8}TiS_3$, a uniaxial material which we found to possess a record birefringence ( ) in a broadband low-loss spectral region between m and at least m, with the optic axis in plane of the samples. Compared to stoichiometric unmodulated $SrTiS_3$, which is expected to have , the extra Sr in $Sr_{9/8}TiS_3$ results in additional electrons that selectively occupy localized anisotropic states (Ti-3), greatly enhancing the polarizability of the material along the optic axis, and thus resulting in a degree of optical anisotropy far larger than has been demonstrated in any bulk material. The atomic-scale structural features of $Sr_{9/8}TiS_3$ were

resolved using single-crystal X-ray diffraction and directly observed with HAADF-STEM imaging, and the resulting structural information was used to perform DFT calculations that clarified the physical mechanism leading to the experimentally observed colossal optical anisotropy. We anticipate that structural modulation in nonstoichiometric crystals will be a new tool in realizing materials with large degrees of optical and optoelectronic anisotropy. Furthermore, the connection between subtle structural modulations and large changes in the refractive index may enable a new class of optical materials that can be tuned with an applied stimulus.

Methods

Crystal growth method

Single crystals of $Sr_{9/8}TiS_3$ were grown via the chemical vapor transport method with iodine as the transporting agent. Starting materials, strontium sulfide powder (Alfa Aesar, 99.9%), titanium powder (Alfa Aesar, 99.9%), sulfur pieces (Alfa Aesar, 99.999%) and iodine pieces (Alfa Aesar 99.99%) were stored and handled in a nitrogen-filled glove box. Stoichiometric quantities (weighed as SrS : Ti : S = 1 : 1 : 2) of precursor powders with a total weight of 1.0 g were mixed and loaded into a quartz tube (19 mm diameter and 2 mm thickness) along with ~0.75 $mg \cdot cm^{-3}$ iodine inside the glove box. The tube was capped with ultra-torr fittings and a quarter-turn plug valve to avoid exposure to air before being evacuated and sealed using a blowtorch. The sealed tube was then loaded in an MTI OTF-1200X-S-II Dual Heating Zone 1200 °C compact split tube furnace, heated to the reaction temperature of 1055 °C at 100 °C/h, and held for 150 hours before cooling down. The temperature gradient in the dual-zone furnace was kept at 5 °C/cm.

Infrared reflection and transmission spectroscopy

Polarization-resolved infrared spectroscopy was carried out using a Fourier transfer infrared spectrometer (Bruker Vertex 70) outfitted with an infrared microscope (Hyperion 2000). A 15× Cassegrain microscope objective (NA = 0.4) was used for both reflection and transmission measurements under normal incidence on the (100) face of a $Sr_{9/8}TiS_3$ crystal. These measurements were performed with a Globar source, a potassium bromide (KBr) beam splitter, and a mercury cadmium telluride (MCT) detector. A wire-grid polarizer was used to control the polarization of the incident light. The samples were maintained at room temperature.

Spectroscopic ellipsometry

Variable-angle spectroscopic ellipsometry measurements were performed using a VASE ellipsometer with focusing probes (J. A. Woollam Co.) over a spectral range of 210 nm to 2500 nm at an angle of incidence of 55°. Data were acquired from three different sample orientations (optical axis parallel,

perpendicular, and 30° to the plane of incidence). Data analysis and refractive index extraction were performed using WVASE software (J. A. Woollam Co.). When creating the optical model, we assumed that the crystal is uniaxial with the *c*-axis along the quasi-1D chains, as implied by our structural characterization in Fig. 2. The samples were maintained at room temperature. More details can be found in *Supplementary Section 2*.

Single-crystal diffraction

Single-crystal diffraction of $Sr_{9/8}TiS_3$ crystals was first collected using the Rigaku XtaLAB AFC12 (RCD3) diffractometer at Oak Ridge National Laboratory. The diffractometer is equipped with a Mo Kα X-ray source (wavelength 0.71073 Å) and a Rigaku HyPix-6000HE detector. Diffraction data were collected using four scans with a step size of 0.5° and a collection time of 25 seconds per step, which achieved a 99.95% completeness (total number of measured peaks divided by the total number of peaks), for a resolution of 0.75 Å.

A larger-size platelet-shaped crystal was characterized in beamline 12.2.1 at the Advanced Light Source (ALS) at Lawrence Berkeley National Laboratory. Crystals were mounted on MiTeGen Dual Thickness MicroMounts™ and placed in a nitrogen cold stream on the goniometer-head of a Bruker D8 diffractometer, which is equipped with a PHOTONII CPAD detector operating in shutterless mode. Diffraction data were collected using synchrotron radiation at a wavelength of 0.72880 Å with silicon (111) monochromator. A combination of and scans with scan speeds of 1 s per 2 degrees for the scans, and 1 s per 0.15 degree for the scans at 2 0 and -20°, respectively, were acquired. 99.95% completeness for a resolution of 0.6 Å was achieved.

Data reduction, scaling and precession map analysis were done in CrysAlisPro and APEX3 corresponding to the original data collection format. Crystal structures were solved and refined in ShelXle[53] and Jana 2020[54].

Electron microscopy

We prepared [001] a cross-sectional TEM lamella using a Thermo Scientific Helios G4 PFIB UXe Dual Beam equipped with an EasyLift manipulator. Standard lift-out technique was used to prepare the TEM lamella. [100]-oriented TEM specimen was prepared using Ar-ion milling (Fischione Model 1010). A 4 keV ion beam with the angle of incidence set at 5° and followed by a 1 keV ion beam with the angle of incidence at 2° was used to thin down the specimen. All the TEM lamellae were heated to 130 °C in vacuum for 8 hours to remove organic contaminants from the surface before being inserted into the microscope column.

Scanning transmission electron microscope (STEM) imaging was performed using an aberration-corrected Nion UltraSTEM 100 operated at 100 kV with a convergence semi-angle of 30 mrad.

HAADF-STEM images were acquired using an annular dark-field detector with inner and outer collection semi-angles of 80 and 200 mrad, respectively.

To interpret the intensity variation in a STEM image, multi-slice simulations were carried out on the structures of $Sr_{9/8}TiS_3$ and hypothetical stoichiometric $SrTiS_3$. The structure of $Sr_{9/8}TiS_3$ was obtained from the structural refinement and the structure of $SrTiS_3$ was obtained after optimization using DFT. STEM-HAADF simulations were performed using the multi-slice method as implemented in μSTEM[55]. Thermal scattering was included in our simulations through the phonon-excitation model proposed by Forbes et al.[56] The sample thickness was set to 15 nm and the defocus value was set to 10 Å to obtain good agreement in intensity profiles with the experimental data. We performed the simulations using an aberration-free probe with an accelerating voltage of 100 kV and a convergence semi-angle of 30 mrad. The inner and outer collection angles for the HAADF detector were set to 80 and 200 mrad, respectively.

Theoretical calculations

We performed density-functional theory (DFT) calculations using projected augmented-wave potentials[57] as implemented in the Vienna Ab initio Simulation Package (VASP)[58,59]. The Perdew-Burke-Ernzerhof (PBE) functional within the generalized gradient approximation (GGA)[60] was used to describe the exchange-correlation interactions. A plane-wave basis with an energy cutoff of 600 eV and an energy convergence criterion of 10^{-8} eV for the electronic convergence were applied. A *k*-point spacing of 0.025 $Å^{-1}$ was chosen for both the structure optimization and total-energy calculation. The criterion for structural optimization was set such that all forces on the atoms were less than 10^{-4} eV/Å. To increase the localization of Ti-3*d* electrons, we used DFT + *U* calculations[51]. An effective on-site Hubbard *U* = 3.0 eV was used for the Ti-*3d* electrons. Furthermore, we considered magnetic configurations for both stoichiometric $SrTiS_3$ ($P2_1$) and modulated $Sr_{9/8}TiS_3$ ($R3c$) lattices. The special quasi-random structure (SQS) model implemented in the alloy theoretic automatic toolkit[61,62] was used to generate best approximations of randomness in the paramagnetic configuration. The visualization of band decomposed charge density was performed for valence electrons within 0.3 eV below Fermi energy. After running convergence tests, we set the total number of energy bands (NBANDS = 736 for primitive cell) to be 2.5 times as many as the number of valence bands for the dielectric function calculations which covers the energy transition up to 62 eV.

Acknowledgements

The work at UW-Madison was supported by ONR, with award no. N00014-20-1-2297. The work at USC and WUStL were supported, in part, by an ARO MURI program with award no. W911NF-21-1-0327, and the National Science Foundation (NSF) of the United States under grant numbers DMR-

2122070 and DMR-2122071. J.R. acknowledges support from the Army Research Office under Award No. W911NF-19-1-0137, and an Air Force Office of Scientific Research grant no. FA9550-22-1-0117. This research used resources of the Advanced Light Source, which is a DOE Office of Science User Facility under contract no. DE-AC02-05CH11231. J.R., B.Z., and H.C. gratefully acknowledge the use of Core Center for Excellence in Nano Imaging (CNI), University of Southern California for some of the sample preparation and characterization studies. R.M. acknowledges NSF for partial support through grant DMR-2145797. M.K. and H.M. acknowledge the use of facilities and instrumentation at the UW-Madison Wisconsin Centers for Nanoscale Technology (WCNT) partially supported by the NSF through the University of Wisconsin Materials Research Science and Engineering Center (DMR-1720415). STEM characterization was performed at the Center for Nanophase Materials Sciences and X-ray structural work at the Spallation Neutron Source, both of which are US Department of Energy, Office of Science User Facility operated by Oak Ridge National Laboratory. This work used computational resources through allocation DMR160007 from the Advanced Cyberinfrastructure Coordination Ecosystem: Services & Support (ACCESS) program, which is supported by NSF grants #2138259, #2138286, #2138307, #2137603, and #2138296.

Author contributions

M.A.K., R.M. and J.R. conceived and supervised the research. H.M., J.S. and M.A.K. identified the large optical anisotropy. G.R., G.Y.J. and R.M. performed the structural modulation studies. H.M. and J.S. performed IR spectroscopy. H.M., J.S. and C.W. performed the ellipsometry studies. B.Z., S.S., and S.N. grew the crystals and performed structural and chemical characterization. B.Z., N.S., S.J.T., and B.C.C. performed single-crystal XRD measurements. G.Y.J., G.R., J.C. and R.M. performed the theoretical calculations. G.R. and A.S.T. performed the STEM experiments and analysis with assistance from J.A.H., M.C., H.C., and R.M. All authors discussed the results. H.M., M.A.K., G.R., B.Z, J.R., and R.M. wrote the manuscript with contributions from all co-authors.

Competing interests

The authors declare no conflict of interest.

Data availability

Data presented in the main text and supplementary information are open access and can be found on Zenodo[63].

Reference

1. Weber, M. F., Stover, C. A., Gilbert, L. R., Nevitt, T. J. & Ouderkirk, A. J. Giant birefringent optics in multilayer polymer mirrors. *Science* **287**, 2451–2456 (2000).
2. Yasuno, Y., Makita, S., Sutoh, Y., Itoh, M. & Yatagai, T. Birefringence imaging of human skin by polarization-sensitive spectral interferometric optical coherence tomography. *Opt. Lett.* **27**, 1803–1805 (2002).
3. Oka, K. & Kaneko, T. Compact complete imaging polarimeter using birefringent wedge prisms. *Opt. Express* **11**, 1510–1519 (2003).
4. Nicholls, L. H. *et al.* Ultrafast synthesis and switching of light polarization in nonlinear anisotropic metamaterials. *Nat. Photon.* **11**, 628–633 (2017).
5. Wu, C. *et al.* Giant optical anisotropy in the UV-transparent 2D nonlinear optical material $Sc(IO_3)_2(NO_3)$. *Angewandte Chemie* **133**, 3506–3510 (2021).
6. de Dood, M. J. A., Irvine, W. T. M. & Bouwmeester, D. Nonlinear photonic crystals as a source of entangled photons. *Phys. Rev. Lett.* **93**, 040504 (2004).
7. Riccardi, M. & Martin, O. J. F. Electromagnetic forces and torques: from dielectrophoresis to optical tweezers. *Chem. Rev.* (2023).
8. Dyakonov, M. New type of electromagnetic wave propagating at an interface. *J. Exp. Theor. Phys.* **94**, 119 (1988).
9. Ma, W. *et al.* In-plane anisotropic and ultra-low-loss polaritons in a natural van der Waals crystal. *Nature* **562**, 557–562 (2018).
10. Chaudhary, K. *et al.* Engineering phonon polaritons in van der Waals heterostructures to enhance in-plane optical anisotropy. *Sci. Adv.* **5**, eaau7171 (2019).
11. Ma, W. *et al.* Ghost hyperbolic surface polaritons in bulk anisotropic crystals. *Nature* **596**, 362–366 (2021).
12. Wang, Q. H., Kalantar-Zadeh, K., Kis, A., Coleman, J. N. & Strano, M. S. Electronics and optoelectronics of two-dimensional transition metal dichalcogenides. *Nat. Nanotech.* **7**, 699–712 (2012).
13. Segura, A. *et al.* Natural optical anisotropy of h-BN: Highest giant birefringence in a bulk crystal through the mid-infrared to ultraviolet range. *Phys. Rev. Mater.* **2**, 024001 (2018).
14. Álvarez-Pérez, G. *et al.* Infrared permittivity of the biaxial van der Waals semiconductor α-MoO_3 from near- and far-field correlative studies. *Adv. Mater.* **32**, 1908176 (2020).
15. Taboada-Gutiérrez, J. *et al.* Broad spectral tuning of ultra-low-loss polaritons in a van der Waals crystal by intercalation. *Nat. Mater.* **19**, 964–968 (2020).
16. Ermolaev, G. A. *et al.* Giant optical anisotropy in transition metal dichalcogenides for next-generation photonics. *Nat. Commun.* **12**, 854 (2021).
17. Bartholin, R. *Experimenta Crystalli Islandici disdiaclastici, quibus mira et insolita refractio detegitur*. (1669).
18. Fresnel, A. Note sur le calcul des teintes que la polarisation développe dans les lames cristallisées. *Annales de chimie et physique* **17**, 101–112 (1821).
19. Fresnel, A. Extrait d'un Mémoire sur la double réfraction. *Annales de chimie et physique* **28**, 263–279 (1825).
20. Bragg, W. L. The refractive indices of calcite and aragonite. *Proceedings of the Royal Society of London. Series A, Containing Papers of a Mathematical and Physical Character* **105**, 370–386 (1924).
21. Bragg, W. L. Atomic structure of minerals. (1937).

22. Lawless, W. N. & Devries, R. C. Oxygen polarizability and point-dipole theory in the carbonate minerals. *J. Phys. Chem. Solids.* **25**, 1119–1124 (1964).
23. Isherwood, B. J. & James, J. A. Structural dependence of the optical birefringence of crystals with calcite and aragonite type structures. *Acta Cryst. A* **32**, 340–341 (1976).
24. Niu, S. *et al.* Giant optical anisotropy in a quasi-one-dimensional crystal. *Nat. Photon.* **12**, 392–396 (2018).
25. Wang, J. & Kovnir, K. Giant anisotropy detected. *Nat. Photon.* **12**, 382–383 (2018).
26. Zhao, B. *et al.* Orientation-controlled anisotropy in single crystals of quasi-1D $BaTiS_3$. *Chem. Mater.* **34**, 5680–5689 (2022).
27. Surendran, M. *et al.* Quasi-epitaxial growth of $BaTiS_3$ films. *J. Mater. Res.* **37**, 3481–3490 (2022).
28. Huang, Y., Fang, Z., Yang, B.-P., Zhang, X.-Y. & Mao, J.-G. A new birefringent material, $HfF_2(IO_3)_2$, with a large birefringence and improved overall performances achieved by the integration of functional groups. *Scripta Materialia* **223**, 115082 (2023).
29. Ermolaev, G. A. *et al.* Giant and tunable excitonic optical anisotropy in single-crystal $CsPbX_3$ halide perovskites. Preprint at https://doi.org/10.48550/arXiv.2210.03541 (2022).
30. Sinton, W. M. Birefringence of rutile in the infrared. *J. Opt. Soc. Am.* **51**, 1309_1-1310 (1961).
31. Ghosh, G. Dispersion-equation coefficients for the refractive index and birefringence of calcite and quartz crystals. *Opt. Commun.* **163**, 95–102 (1999).
32. Luo, H. T., Tkaczyk, T., Dereniak, E. L., Oka, K. & Sampson, R. High birefringence of the yttrium vanadate crystal in the middle wavelength infrared. *Opt. Lett.* **31**, 616–618 (2006).
33. Zelmon, D. E., Small, D. L. & Jundt, D. Infrared corrected Sellmeier coefficients for congruently grown lithium niobate and 5 mol. % magnesium oxide–doped lithium niobate. *J. Opt. Soc. Am. B* **14**, 3319–3322 (1997).
34. Guoqing, Z. *et al.* Growth and spectrum of a novel birefringent α-BaB_2O_4 crystal. *J. Cryst. Growth* **191**, 517–519 (1998).
35. Chenault, D. B. & Chipman, R. A. Infrared birefringence spectra for cadmium sulfide and cadmium selenide. *Appl. Opt.* **32**, 4223–4227 (1993).
36. Dodge, M. J. Refractive properties of magnesium fluoride. *Appl. Opt.* **23**, 1980–1985 (1984).
37. Nikogosyan, D. N. *Nonlinear optical crystals: a complete survey*. (Springer Science & Business Media, 2006).
38. Niu, S. *et al.* Bandgap control via structural and chemical tuning of transition metal perovskite chalcogenides. *Adv. Mater.* **29**, 1604733 (2017).
39. Niu, S. *et al.* Mid-wave and long-wave infrared linear dichroism in a hexagonal perovskite chalcogenide. *Chem. Mater.* **30**, 4897–4901 (2018).
40. Tranchitella, L. J., Fettinger, J. C., Dorhout, P. K., Van Calcar, P. M. & Eichhorn, B. W. Commensurate columnar composite compounds: synthesis and structure of $Ba_{15}Zr_{14}Se_{42}$ and $Sr_{21}Ti_{19}Se_{57}$. *J. Am. Chem. Soc.* **120**, 7639–7640 (1998).
41. Loye, H.-C. zur, Zhao, Q., E. Bugaris, D. & Michael Chance, W. 2*H*-perovskite related oxides: Synthesis, structures, and predictions. *CrystEngComm* **14**, 23–39 (2012).
42. Gourdon, O., Petricek, V. & Evain, M. A new structure type in the hexagonal perovskite family; structure determination of the modulated misfit compound $Sr_{9/8}TiS_3$. *Acta Cryst. B* **56**, 409–418 (2000).

43. Gourdon, O. *et al.* Influence of the metal–metal sigma bonding on the structures and physical properties of the hexagonal perovskite-type sulfides $Sr_{9/8}TiS_3$, $Sr_{8/7}TiS_3$, and $Sr_{8/7}[Ti_{6/7}Fe_{1/7}]S_3$. *J. Solid State Chem.* **162**, 103–112 (2001).
44. Yamamoto, A. Crystallography of quasiperiodic crystals. *Acta Cryst. A* **52**, 509–560 (1996).
45. Onoda, M., Saeki, M., Yamamoto, A. & Kato, K. Structure refinement of the incommensurate composite crystal $Sr_{1.145}TiS_3$ through the Rietveld analysis process. *Acta Cryst. B* **49**, 929–936 (1993).
46. International Tables for Crystallography. *urn:isbn:978-1-4020-4969-9* https://it.iucr.org/ doi:10.1107/97809553602060000001.
47. Stokes, H. T., Campbell, B. J. & van Smaalen, S. Generation of (3 + *d*)-dimensional superspace groups for describing the symmetry of modulated crystalline structures. *Acta Cryst. A* **67**, 45–55 (2011).
48. Pennycook, S. J. & Jesson, D. E. High-resolution Z-contrast imaging of crystals. *Ultramicroscopy* **37**, 14–38 (1991).
49. Thind, A. S., Huang, X., Sun, J. & Mishra, R. First-principles prediction of a stable hexagonal phase of $CH_3NH_3PbI_3$. *Chem. Mater.* **29**, 6003–6011 (2017).
50. Wagner, N., Seshadri, R. & Rondinelli, J. M. Property control from polyhedral connectivity in ABO_3 oxides. *Phys. Rev. B* **100**, 064101 (2019).
51. Dudarev, S. L., Botton, G. A., Savrasov, S. Y., Humphreys, C. J. & Sutton, A. P. Electron-energy-loss spectra and the structural stability of nickel oxide: An LSDA+U study. *Phys. Rev. B* **57**, 1505–1509 (1998).
52. Gajdoš, M., Hummer, K., Kresse, G., Furthmüller, J. & Bechstedt, F. Linear optical properties in the projector-augmented wave methodology. *Phys. Rev. B* **73**, 045112 (2006).
53. Hübschle, C. B., Sheldrick, G. M. & Dittrich, B. *ShelXle*: a Qt graphical user interface for *SHELXL*. *J Appl. Cryst.* **44**, 1281–1284 (2011).
54. Petříček, V., Dušek, M. & Palatinus, L. Crystallographic computing system JANA2006: General features. *Zeitschrift für Kristallographie - Crystalline Materials* **229**, 345–352 (2014).
55. Allen, L. J., D′Alfonso, A. J. & Findlay, S. D. Modelling the inelastic scattering of fast electrons. *Ultramicroscopy* **151**, 11–22 (2015).
56. Forbes, B. D., Martin, A. V., Findlay, S. D., D'Alfonso, A. J. & Allen, L. J. Quantum mechanical model for phonon excitation in electron diffraction and imaging using a Born-Oppenheimer approximation. *Phys. Rev. B* **82**, 104103 (2010).
57. Blöchl, P. E. Projector augmented-wave method. *Phys. Rev. B* **50**, 17953–17979 (1994).
58. Kresse, G. & Furthmüller, J. Efficiency of ab-initio total energy calculations for metals and semiconductors using a plane-wave basis set. *Comput. Mat. Sci.* **6**, 15–50 (1996).
59. Kresse, G. & Furthmüller, J. Efficient iterative schemes for ab initio total-energy calculations using a plane-wave basis set. *Phys. Rev. B* **54**, 11169–11186 (1996).
60. Perdew, J. P., Burke, K. & Ernzerhof, M. Generalized gradient approximation made simple. *Phys. Rev. Lett.* **77**, 3865–3868 (1996).
61. Zunger, A., Wei, S.-H., Ferreira, L. G. & Bernard, J. E. Special quasirandom structures. *Phys. Rev. Lett.* **65**, 353–356 (1990).
62. van de Walle, A. *et al.* Efficient stochastic generation of special quasirandom structures. *Calphad* **42**, 13–18 (2013).
63. Mei, H. *et al.* Colossal optical anisotropy from atomic-scale modulations: manuscript data. (2023) doi:10.5281/zenodo.7577670.

Subtle atomic-scale structural modulations of a crystal can dramatically change its optical properties. Single-crystal plates of **modulated quasi-1D chalcogenide $Sr_{9/8}TiS_3$** is shown to have a record in-plane birefringence ( ) within a broad transparent window in the mid- to far-infrared. Structural modulation will be a new tool in realizing materials with large degrees of optical and optoelectronic anisotropy.